

Cracking and crackling in concrete-like materials: A dynamic energy balance



A. Carpinteri, G. Lacidogna*, M. Corrado¹, E. Di Battista

Department of Structural, Geotechnical and Building Engineering, Politecnico di Torino, Italy

ARTICLE INFO

Article history:

Received 30 July 2015

Received in revised form 15 December 2015

Accepted 11 January 2016

Available online 29 January 2016

Keywords:

Quasi-brittle fracture

Acoustic emission

Signals attenuation

Energy emitted

Energy dissipated

Energy released

Cohesive crack model

ABSTRACT

An analysis of the Acoustic Emission (AE) activity and of the energy fields is carried out with reference to three-point bending (TPB) tests on concrete beams with different sizes. First, a cracking mode classification is performed on the basis of AE parameters like the average frequency and the rise angle of the waveforms. A compression test is also performed to verify if the identification of the fracture mode by means of the AE parameters is appropriate. Then, regarding the TPB tests, the fracture energy (dissipated) and the energy detected by the AE sensors (emitted) per unit of fracture surface are compared. The former energy increases with the specimen size whereas the latter one decreases. Therefore, a direct relation cannot be established between the two forms of energy, although an indirect relationship is given by the fact that their sum corresponds to the total energy released during the test.

© 2016 Elsevier Ltd. All rights reserved.

1. Introduction

The Acoustic Emission (AE) technique is currently used during experimental tests to investigate on the damage evolution in ductile or brittle materials before the final failure [1,2]. The spatio-temporal evolution of ultrasonic AE signals, also known as “*crackling noise*” when they occur in the audible field, is a direct result of cracking bonds during the fracture of materials. The AE time-series are characterized by silent intervals separated by events of varying length and amplitude, that involve the emission of different energy levels. For these reasons, this non-destructive monitoring method is useful for studying the critical phenomena and to predict the durability and remaining life-time in full-scale structures [3,4].

According to this technique, it is possible to detect the transient elastic waves related to each stress-induced crack propagation event inside a material. These waves can be captured and recorded by transducers applied on the surface of specimens or structural elements. The transducers are piezoelectric sensors that transform the energy of the elastic waves into electric signals. A suitable analysis of the AE waveform parameters (peak amplitude, duration time and frequency) permits to obtain a detailed information about the damage evolution, such as the cracking pattern, the released energy, the prevalent fracture mode, and the achievement of the critical conditions that anticipate the collapse. The last analysis can be performed by calculating the *b*-value from the Gutenberg-Richter (GR) law. Even though two different dimensional scales are involved, the GR law can be applied in the same way for earthquake distributions in seismic areas as well as for the structural monitoring by the AE technique [5–7].

* Corresponding author. Tel.: +39 011 090 4871; fax: +39 011 090 4899.

E-mail address: giuseppe.lacidogna@polito.it (G. Lacidogna).

¹ Present address: Civil Engineering Institute, Materials Science and Engineering Institute, Ecole Polytechnique Fédérale de Lausanne (EPFL), Station 18, CH-1015 Lausanne, Switzerland.

The connection between fracture mode and recorded waves depends on different factors like geometric conditions, relative orientations, and propagation distances [8]. The identification of the cracking mode may be done with the AE wave's rise time (which is the time interval between the wave onset and its maximum amplitude), the value of the peak amplitude, and the Average Frequency (AF). The ratio between the rise time (expressed in ms) and the peak amplitude (expressed in V) defines the Rise Angle (RA), as shown in Fig. 1 [9–11]. The peak amplitude can be also expressed in dB by the equation:

$$A[\text{dB}] = 20 \cdot \text{Log}_{10} \left(\frac{V}{V_0} \right), \quad (1)$$

where V is the amplitude of the signal in volt, and V_0 is the maximum amplitude of the background noise.

The AF, measured in kHz, is obtained from the AE ring-down count divided by the duration time of the signal. The AE ring-down count corresponds to the number of threshold crossings within the signal duration time [9–11].

The fracture mode is then characterized by the shape of the AE waveforms: low RAs and high AFs are typical for tensile crack propagations which consist in opposite movements of the crack surfaces (Mode I), whereas shear events (Mode II) usually generate longer waveforms, with higher RAs and lower AFs, as shown in Fig. 1 [12–15]. Variations in the RA and AF values during the loading process identify a change in the prevalent failure mode of the specimen.

In general, a decrease in frequency might be also caused by the formation of large cracks during both tensile and shearing processes. In fact, it is reasonable to assume that high frequency waves are generated from small discontinuities, that characterize the beginning of the damage process, whereas low frequency ones can be produced only from large cracks, that usually develop during the final collapse [16].

Another interesting feature of the AE signals is that they can give insights on the process of energy dissipation and emission during the loading process. In this context, experimental analyses have evidenced that the scaling of the cumulative number of AE events by varying the specimen dimension can be profitably used to determine the physical dimension of the damage domain in disordered materials. The total number of AE events at the end of the test in fact varies with the specimen size according to a power-law having a noninteger exponent that is directly related to the fractal character of the damage domain [3,17]. Alternatively, the characterization of the damage domain can be also obtained by means of a statistical analysis of the distribution of AE events in a single test [17]. From the viewpoint of energy dissipation and emission, the cumulative number of AE events and the energy content of the AE events are usually correlated to the mechanical energy dissipated during the complete failure process, namely fracture energy in tension and crushing energy in compression [18,19]. However, recent studies carried out by Carpinteri and co-workers focusing on the catastrophic failure of rock specimens in compression have suggested that such a correlation is not always correct [20]. In particular, it was evidenced that a large amount of AE activity takes place during the post-peak snap-back instability. The typical shape of the load vs. displacement curve, when the global unstable behavior is fully captured, e.g. by controlling the compression test by means of the circumferential expansion instead of the longitudinal deformation, is that shown in Fig. 2a. However, this very brittle mechanical response can be observed also under tension and bending loading conditions, when brittle materials are tested in large and/or slender specimens. The behavior shown in Fig. 2a is consequent to the fact that the energy dissipated through material damage is less than all the elastic energy stored in the body. In this case, the portion of energy that is not dissipated by material damage (area E in Fig. 2a) is abruptly emitted leading to dynamic vibrations, with propagation of elastic waves. Of course, this portion of energy will be also dissipated, although through material viscosity, impacts of fragments, and heat. From the diagram in Fig. 2a, therefore, three different energy components can be distinguished: the energy dissipated by material damage (gray area), the surplus of elastic energy with respect to the dissipated one (red¹ dashed area), and the total released energy, which is the sum of the two previous areas. When a catastrophic failure occurs, the AE energy seems to be correlated to the surplus of elastic energy [20]. Accordingly, such an energy component can be referred to as emitted energy.

Certainly, global snap-back instabilities take place only under specific conditions (large sizes and slendernesses, and/or brittle materials), whereas in most of the cases a more stable response, represented by a softening behavior, is obtained. However, even in such cases, local discontinuities, which are an indication of snap-back or snap-through instabilities, are usually noticed in heterogeneous materials such as aggregative and fiber-reinforced materials. Such local phenomena, that are evident at a microscale level, are due to the fact that cracks grow in a discontinuous manner, with sudden propagations and arrests due to the bridging action of the secondary phases as well as by the rise and coalescence of microcracks in the process zone [21,22]. A load–displacement curve representative of a global softening behavior perturbed by multiple local instabilities is shown in Fig. 2b. Each drop in the load carrying capacity occurring in the post-peak phase is related to a sudden crack propagation due, for instance, to the rupture of a reinforcing fiber. Then, the load carrying capacity is partially recovered following a path with a reduced stiffness. From the energetic point of view, each local instability is due to the emission of a surplus of elastic energy, which is not dissipated by the material damage (dashed areas in Fig. 2b). This emitted energy can be detected by the AE sensors.

In the present paper, the AE parameters acquired during three-point bending tests on notched concrete beams and a compression test on a cylindrical specimen are analyzed. These analyses are performed in order to identify the dominant fracture mode and to investigate on the evolution of the released, dissipated and emitted energies during the test and on their mutual correlations. The released energy is the total elastic energy stored in the body during loading and discharged by the cracking

¹ For interpretation of color in Figs. 2 and 18, the reader is referred to the web version of this article.

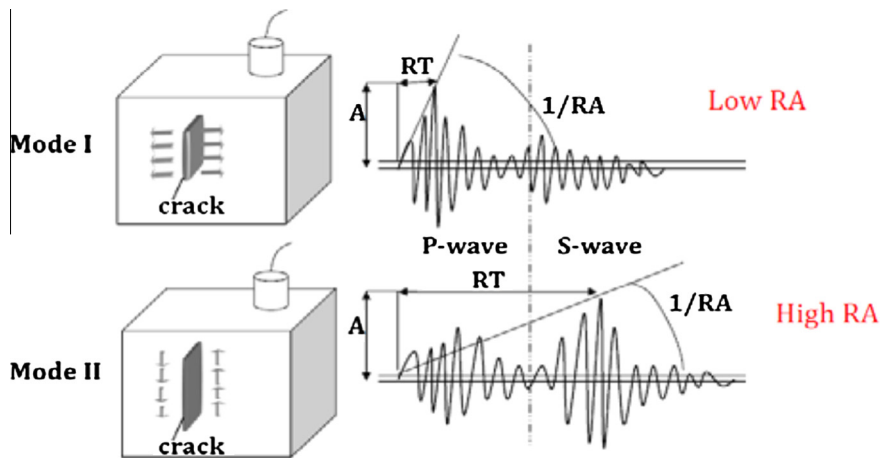


Fig. 1. Typical waveforms for tensile and shear events. A is the amplitude and RT the rise time (time between the onset and the point of maximum amplitude) of the waveforms [12–15].

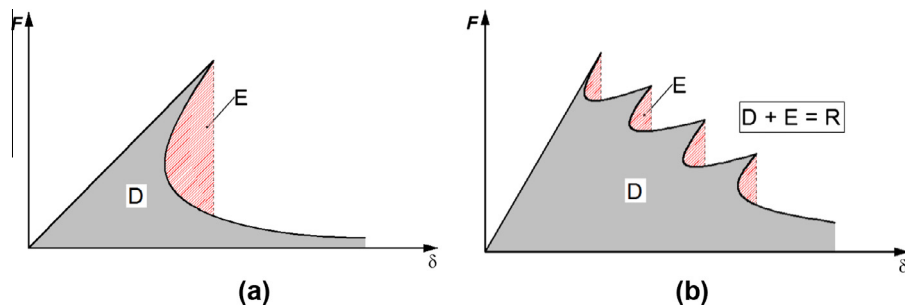


Fig. 2. Load–displacement curves representing: (a) a catastrophic failure (single snap-back); (b) a global softening behavior perturbed by multiple local instabilities (snap-back). The gray areas identify the dissipated energy, D , whereas the dashed ones represent the emitted energy, E . The total released energy, R , is the summation of the two previous areas: $D + E = R$.

process, the dissipated energy includes the energy dissipated by all the material damaging phenomena such as micro-cracking, coalescence of micro-cracks and formation of the traction-free crack, and the emitted energy is the difference of the two previous ones. The dissipated energy is determined both directly from the experimental load–displacement curves and by the cohesive crack model. As far as the emitted energy is concerned, its estimation is obtained from the energy of the AE signals detected by the sensors. In particular, two sensors have been applied to each specimen, placed at different distances from the notch to evaluate how the transient waves from the same damage event change with the distance between the source and the receiver. The proposed comparisons between the dissipated and the emitted energies, carried out both in terms of their cumulative values at the end of the tests and of the evolution of their rates during the loading process, suggest that there is no direct correlation between them.

2. Experimental tests

2.1. Three-point bending tests

Three plain concrete beams with different dimensions have been tested in a three-point bending (TPB) scheme (Fig. 3). The main geometrical parameters are reported in Table 1. The three beams belonged to a wider experimental campaign that was designed following the RILEM recommendations for the evaluation of the fracture energy in concrete [23]. One of the objective was to analyze concrete mixes with different aggregate sizes. In particular, three different mixes were chosen, with maximum aggregate size varying from 15 to 45 mm. In such a case, the Standard specifies the dimensions of the beam as a function of the maximum aggregate diameter: the larger is the maximum aggregate size the larger is the beam. However, the three concrete mixes were designed with the same nominal average compression strength, equal to 25 MPa. All the beams were pre-notched after curing for a depth equal to half the overall height.

The specimens were subjected to TPB tests according to the RILEM Technical Committee TC-50 specifications [23]. The experimental tests were conducted using a servo-hydraulic MTS testing machine (Fig. 4). The samples were tested up to final

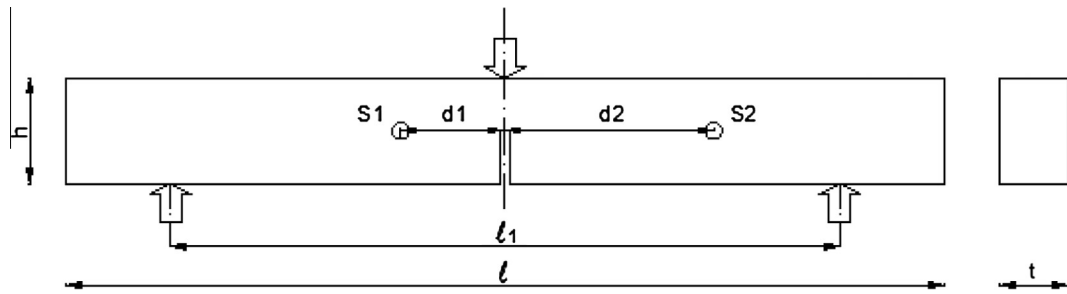


Fig. 3. Schematic representation of the experimental setup. S_1 and S_2 are the sensors applied to detect the AE signals.

Table 1
Main geometrical parameters of the beams.

	Specimen		
	B1	B2	B3
l (mm)	840	1190	1450
h (mm)	100	200	300
t (mm)	100	100	150
l_1 (mm)	800	1140	1180
d_1 (mm)	40	150	200
d_2 (mm)	110	300	400



Fig. 4. Experimental set up of the three-point bending test.

failure by controlling the crack mouth opening displacement (CMOD) with an opening velocity equal to 0.002 mm/s. Moreover, also the vertical deflection, δ , at the centerline of the beams was measured.

During the tests, each specimen was monitored by the AE technique. The AE signals were detected by two piezoelectric transducers, S_1 and S_2 , attached on the surface of the concrete specimen (Fig. 3). The sensors were positioned on the left and right sides of the notch. The distances of the two sensors, d_1 and d_2 , are reported in Table 1 for the three specimens. The sensors, sensitive in the frequency range from 80 to 400 kHz for high-frequency AEs detection, were produced by LEANE NET s.r.l. (Italy). The connection between sensors and acquisition device was realized by coaxial cables in order to reduce the effects of electromagnetic noise. The sampling frequency of recording waveforms was set to 1 Msample/s. The data were collected by a National Instruments digitizer with a maximum of 8 channels. The AE signals captured by the sensors, setting the acquisition threshold level of up to 5 mV, were first amplified up to 40 dB (see Eq. (1)), and then processed.

2.2. Compression test

A compression test was also performed to verify that the identification of the fracture mode by means of the relationship between RA and AF is appropriate. In particular, a cylindrical concrete specimen with diameter equal to 80 mm and length equal to 160 mm was subjected to compression up to the final collapse by means of a servo-hydraulic testing machine. The compression strength resulted to be equal to 69.6 MPa. The specimen was arranged between the press platens without the interposition of friction-reducer layers. Due to the expected brittle response, the test was conducted by imposing a fixed



Fig. 5. Experimental set up of the compression test on the cylindrical concrete specimen.

velocity (0.002 mm/s) to the circumferential expansion. To this aim, the circumferential strain was measured by means of an extensometer attached to a linked chain placed around the cylinder at mid-height (Fig. 5). This control permits to completely detect the load–displacement curve, even in the case of severe unstable phenomena such as snap-back. Due to the limited dimension of the specimen, AE detection was performed by means of a single sensor, applied on the lateral surface of the sample.

3. Identification of the fracture mode by AE parameters

In this section, the results of the TPB tests carried out on the concrete beams and those of the compression test are presented.

The AE data acquisition procedure used during the tests was based on the total number of hits detected by each sensor, but the AE analysis was limited only to the AE events. An hit is one AE transient signal received by a sensor, whereas one event is a couple of AE hits detected from a single source by the two receivers, the spatial coordinates of which are known [9]. In this way, it is possible to compare each signal captured by the first receiver with the same recorded by the second one, even if they have different distances from the source.

For each beam, the average values of the AE signals parameters recorded by the first sensor have been compared to those of the second sensor.

3.1. AE parameters from three-point bending tests

The load vs. time diagram for the three beams are shown in Figs. 6–8. In those figures, the AFs and the RAs of each AE event (i.e. calculated for each pair of signals, and averaged on the couple of signals received by the two sensors), as well as the cumulated number of AE events are also represented. From a mechanical point of view, the overall behavior of the three specimens is characterized by a softening post-peak branch with negative slope. As far as the AE activity is concerned, the total number of events increases with the specimen size, whereas a similar cumulative curve through the time is obtained. In all of the considered cases, a slight decrease in the AFs by approaching the final stage of the test has been evidenced.

The phenomenon of signal attenuation, due to the wave propagation through an inhomogeneous medium, is analyzed by comparing the mean values of the amplitudes and the AFs of the signals received by the two sensors. The average values of the peak amplitude vs. distance between the acoustic sources and the AE sensor, for the three performed bending tests, are shown in Fig. 9a. The distances between the sensors and the beams notches were selected to obtain data in a range within 40 and 400 mm, and to have more values for distances between 40 and 200 mm. This choice was done in order to verify whether, due to the concrete attenuation properties, there is a more rapid decrease of the signal amplitudes in the vicinity of the AE source. From the experimental data, by increasing the distance, a shift in amplitudes from 66 dB to 56 dB is found, and a linear decrease proportional to the signals propagation length is observed (the slope of the regression line is equal to 0.029) regardless of the test specimen size. As it is well known [1], the AE signal amplitude attenuation is generally represented by a negative exponential function dependent on the signal frequency, propagation distance, and AE wave velocity. In our case the data are well fitted by a linear regression because the detected frequencies are relatively low, from 50 to 70 kHz, and the range of the propagation distances from the AE sources and the sensors is restricted, between 40 and 400 mm. Therefore, only a limited portion of the exponential law is explored, for which the linear regression function represents the tangent line near the origin. Anyhow, it should be emphasized that the correct interpretation of the material attenuation properties also depends on the sensitivity of the AE transducers and on the signals amplification. Trends for the attenuation function similar to that obtained in the present work were also found in [24].

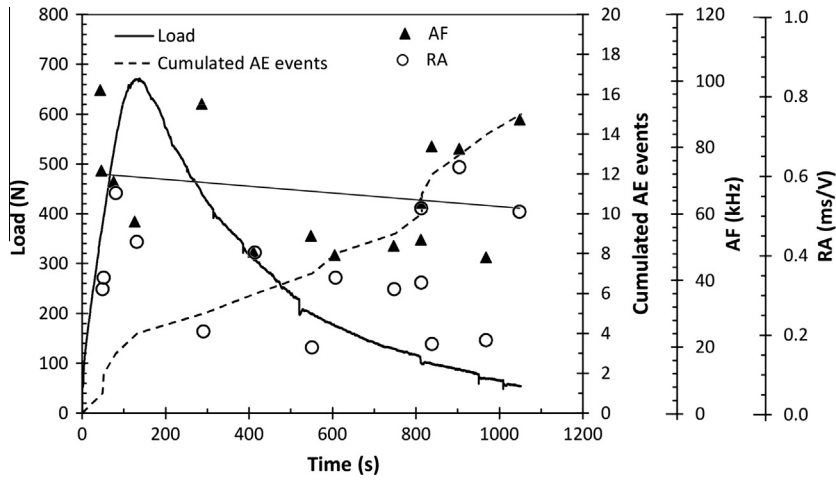


Fig. 6. Specimen B1 (840 × 100 × 100 mm): load vs. time curve, AF and RA values of the detected AE events, and cumulated diagram of the AE events. The straight line represents the linear regression of the AF values during the test.

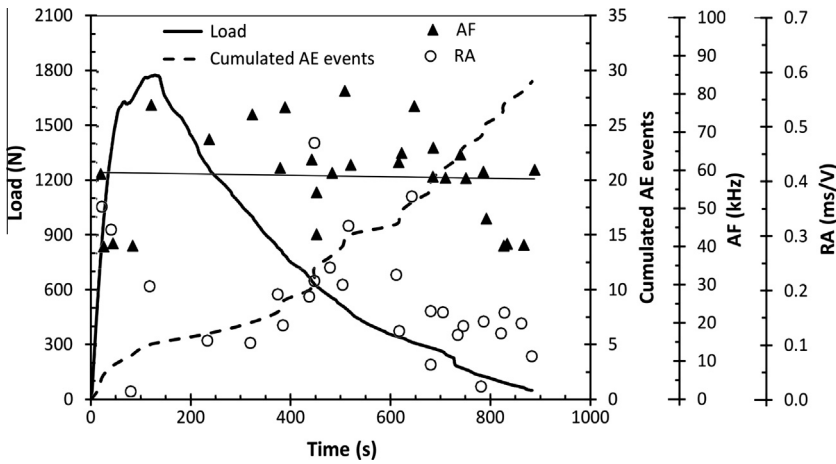


Fig. 7. Specimen B2 (1190 × 200 × 100 mm): load vs. time curve, AF and RA values of the detected AE events, and cumulated diagram of the AE events. The straight line represents the linear regression of the AF values during the test.

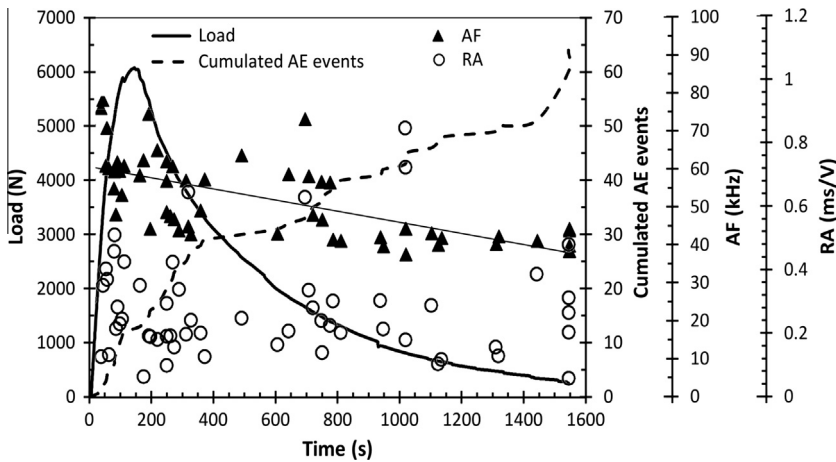


Fig. 8. Specimen B3 (1450 × 300 × 150 mm): load vs. time curve, AF and RA values of the detected AE events, and cumulated diagram of the AE events. The straight line represents the linear regression of the AF values during the test.

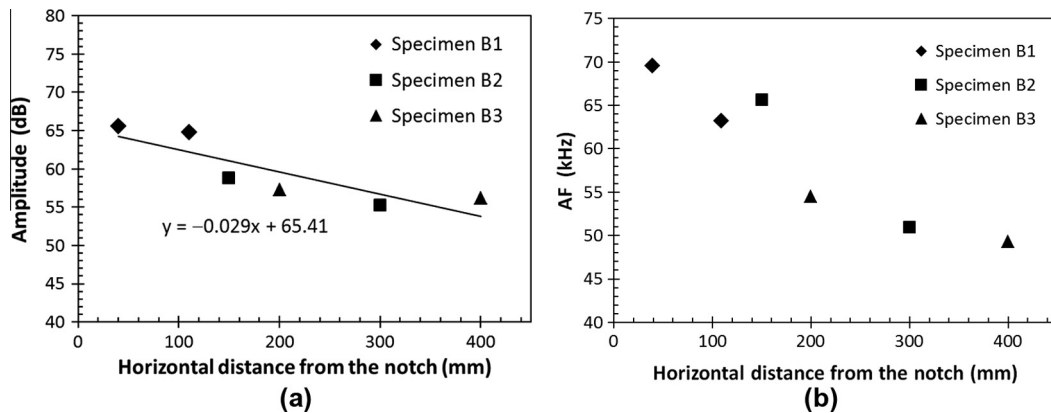


Fig. 9. (a) Average amplitude values and (b) mean AF values vs. distance between crack surface and AE sensor for the three bending specimens.

The mean value of the AFs as a function of the distance between the acoustic sources and the AE sensor, for the three performed bending tests, are shown in Fig. 9b. Globally, a shift in the frequencies from 69.5 to 49.0 kHz is evidenced by increasing the distance of the sensor from 40 to 400 mm. Analogously, also the average value of the RA decreases by increasing the distance of the sensor from the crack. For the considered tests, it ranges between 0.37 and 0.15 ms/V.

The fracture mode was analyzed by means of the relationship between RA and AF values estimated for each sensor, as shown in Fig. 10. In these diagrams, the limits for the AF and RA axes are defined independently for each case, according to each range of data. Considering that a slight decrease in the AFs by approaching the final stage of the test is obtained, and that the RA values are all lower than 1 ms/V, a dominant presence of tensile cracks characterizes the damage evolution up to the final collapse [8,11,12]. However, also a limited amount of Mode II cracks appears, due to local mixed mode crack propagations around inhomogeneities [25,26].

3.2. AE parameters from the compression test

The load vs. time curve for the compression test is reported in Fig. 11. In the same figure the AF and RA values of the detected signals, and the cumulated diagram of the AE events are also represented.

The analysis of the AE data in the AF vs. RA field evidences a dominant presence of Mode I cracks in the first phase of the test, from the beginning up to 1000 s (Fig. 12a). During a second phase, up to 2500 s, the RA values increase although the prevalent cracking mode is still the opening mode (Fig. 12b). Finally, from 2500 s up to the end of the test (about 3800 s), a further increase in the RA values is observed. At the same time, a shift from higher to lower frequencies takes place, involving both tensile cracks (low RA) and shear cracks (high RA), as shown in Fig. 12c. Therefore, the collapse of the specimen is reached by different modalities of fracture: Mode I splitting failure dominates the mechanical response, whereas a crushing mode, characterized also by friction components [3], appears by approaching the final stage (Fig. 12d).

4. Dissipated vs. emitted energy

The total mechanical energy dissipated by the fracture process in the considered TPB tests was evaluated according to the RILEM Recommendations [23]. The obtained results are reported in Table 2, where the corresponding values of the fracture energy, computed as the ratio between the total dissipated energy and the ligament area, are also shown. A considerable increase in the fracture energy was evidenced by increasing the specimen size. This is partially due to the well-known scale effects on the toughness of quasi-brittle materials [27], as well as to the variation in the maximum aggregate diameter of the concrete mix with the beam size (see Section 2.1). The increase in the maximum aggregate diameter, in fact, augments the tortuosity of the crack path, with a consequent increment in the apparent fracture energy. The combined effect of these two phenomena is confirmed by the fact that the increase in the fracture energy with the specimen size can be described by a power-law having an exponent equal to 0.64 (see the diagram in bi-logarithmic scale shown in Fig. 13), whereas extended analyses carried out in the past to assess the validity of the fractal approach to describe the size effects on the fracture energy in concrete-like materials (aggregate diameter being constant) have evidenced values for this exponent in the range between 0.20 and 0.30 [28].

The energy of the AE signals detected during the tests was also evaluated for the three beams. This energy, in accordance with the RILEM TC 212-ACD Recommendations, was calculated as the waveform envelope area of each signal [9]. The values of the total emitted AE energy at the end of the three tests are reported in Table 2. It is worth noting that, since the evaluation of the AE energy is affected by the phenomenon of signal attenuation, the values have been corrected according to the attenuation law derived from Fig. 9a. The problem of the signal amplitude attenuation due to distance is to be taken seriously into

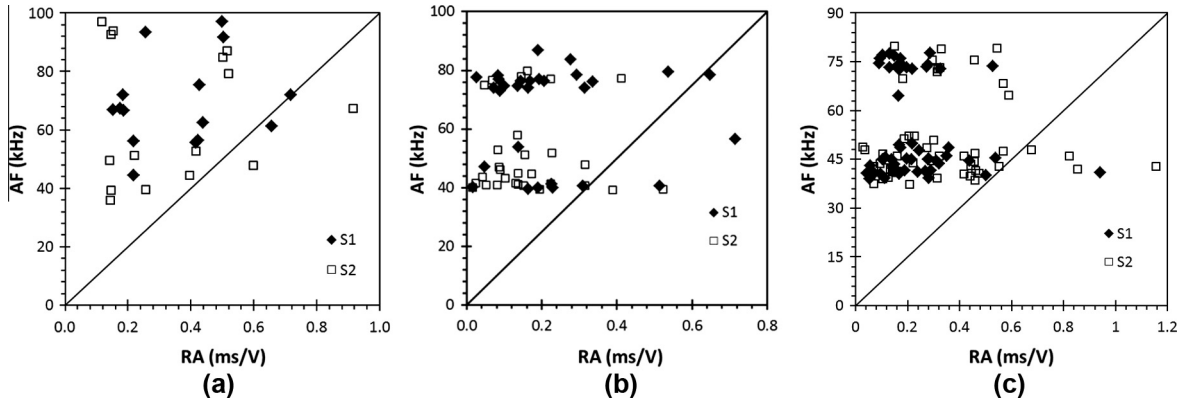


Fig. 10. Fracture mode identification by means of the relationship between RA and AF values for (a) Specimen B1; (b) Specimen B2; and (c) Specimen B3.

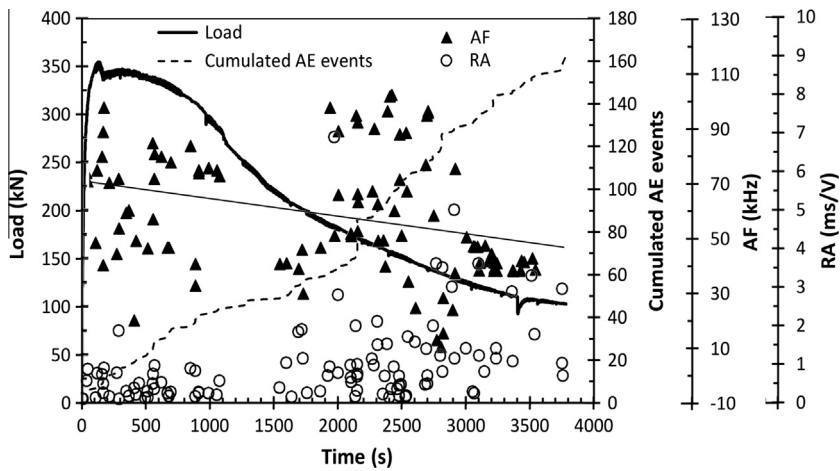


Fig. 11. Compression test: load vs. time curve, AF and RA values of the detected AE events, and cumulated diagram of the AE events. The straight line represents the linear regression of the AF values during the test.

account especially when large structures are monitored. It can be solved only by arranging several sensors to cover large monitored areas [4]. In the same table, the corrected AE energy divided by the ligament area, i.e. the area of the initially intact portion of the mid-span cross section, is also reported. As clearly evidenced by the diagrams in Fig. 13, the AE energy per surface unit decreases by increasing the specimen size, exhibiting, therefore, an opposite trend compared to that of the fracture energy. Such a discrepancy confirms that there is no direct correlation between the two parameters. According to the interpretation proposed in [20], the AE energy should be correlated to the surplus of elastic energy with respect to the dissipated one, that is emitted in correspondence of unstable behaviors (red dashed areas in the diagrams in Fig. 2). The process of crack propagation in concrete is in fact characterized by discontinuous crack growths, with sudden propagations and arrests, due to the presence of microcracks and voids inside the cement matrix, as well as to the bridging effect exerted by the aggregates. The resulting load–displacement curve is therefore similar to that shown in Fig. 2b, even if less pronounced. Some of the local instabilities occurring during the post-peak regime of Specimen B1 are evidenced in Fig. 14. The more marked the instabilities are, the higher the emitted energy, and therefore the acoustic emission activity, is.

4.1. Dissipated and emitted energy rates

The differences between dissipated and emitted energies are herein analyzed on the basis of the evolution of this two quantities over the time, during the progress of the experimental test. To this purpose, their rate, defined as the amount of energy per second, was computed for the three performed tests. As regards the rate of the AE energy, it was directly derived from the results of the monitoring activity carried out during the tests. On the other hand, the rate of the dissipated energy was assessed both from the experimental results and by means of an accurate numerical simulation of the fracturing

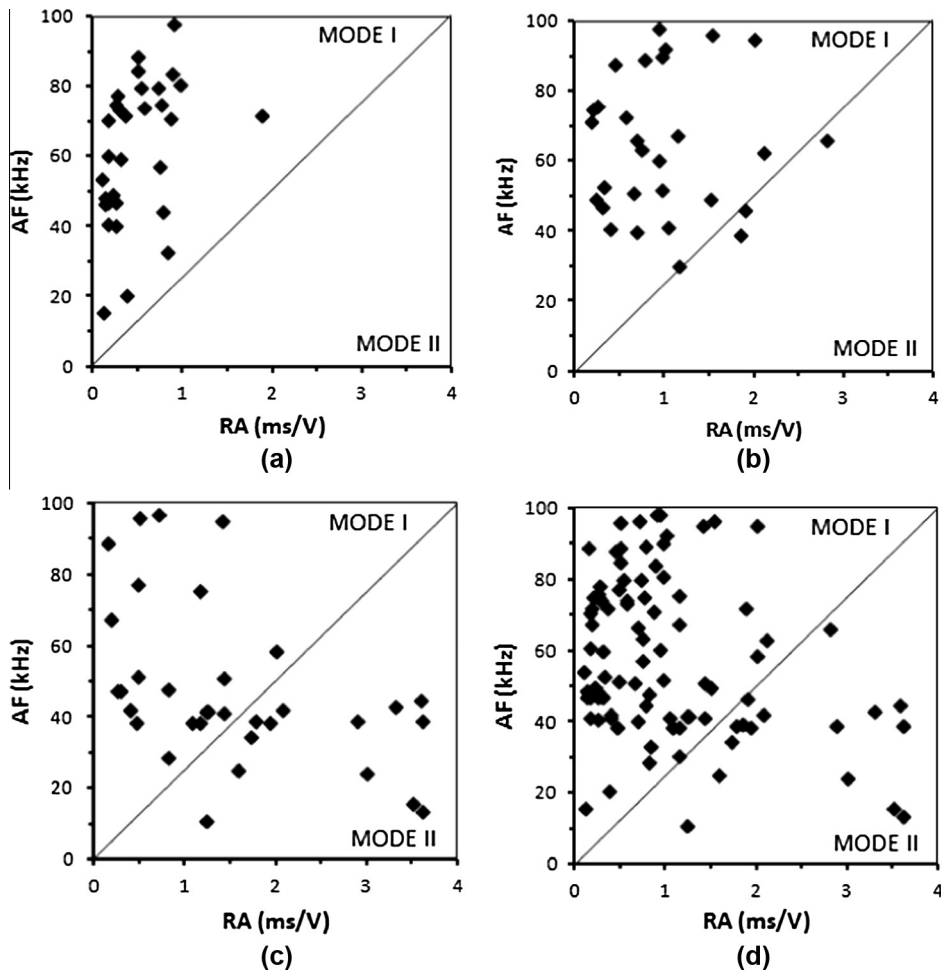


Fig. 12. Fracture mode identification by means of the relationship between RA and AF values for the concrete specimen under compression: (a) from 0 to 1000 s; (b) from 1000 s to 2500 s; (c) from 2500 s to the end of the test; (d) total duration of the test.

Table 2

Total dissipated energy W , fracture energy G_F , released AE energy, and AE energy per surface unity for the three beams.

	Specimen		
	B1	B2	B3
W (J)	0.59	1.73	5.42
G_F (N/m)	118	173	241
AE energy (ms V)	589	930	1494
Corrected AE energy (ms V)	589	1038	1712
Corrected AE energy/ligament (ms V/m ²)	117,800	103,800	76,089

process. In the former case, the evolution of the energy dissipation was evaluated on the basis of the load vs. time and load vs. displacement curves, according to the following procedure, that is also graphically described in Fig. 15:

1. the load corresponding to the overcoming of the elastic limit, after which energy dissipation takes place, is estimated in the load vs. displacement curve (Fig. 15b);
2. the point corresponding to the elastic limit is reported into the load vs. time diagram that, starting from the corresponding time value, is subdivided into several parts, one every second (Fig. 15a);
3. the load values corresponding to the subdivisions are reported back into the load vs. displacement curve, where the areas representing the energy dissipated for each second are defined by means of segments drawn parallelly to the elastic branch. The contribution of the self-weight is also added, by applying a translation of the reference system, as shown in Fig. 15b.

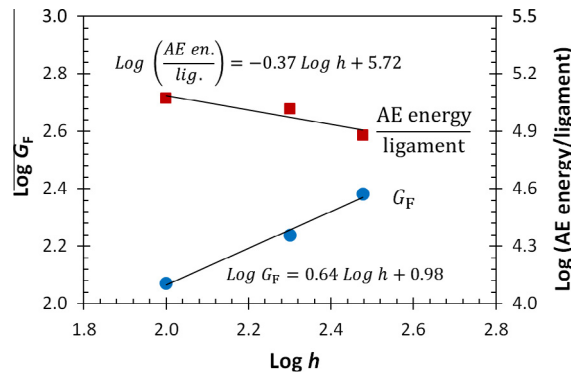


Fig. 13. Bi-logarithmic scale diagrams of the fracture energy and the AE energy per surface unit vs. the beam height.

In the second proposed approach, the fracturing process is modeled by means of a numerical algorithm based on the cohesive crack model, and the dissipated energy is evaluated in terms of the step-by-step variation of the cohesive tractions and of the relative opening displacements along the crack profile. The advantage of such an approach is that the energy dissipation is directly analyzed in relation to the crack propagation process, which is, in fact, the phenomenon responsible for the mechanical energy dissipation. The numerical algorithm originally proposed by Carpinteri [29] for plain concrete beams, and more recently extended by Carpinteri and co-workers [30] to deal also with reinforced concrete elements, is herein adopted.

According to such an approach, the concrete beam is modeled as constituted by two parts exhibiting an elastic behavior and connected in correspondence of the mid-span cross-section, where the crack propagation is allowed. The algorithm is based on a discrete form of the elastic equations governing the mechanical response of the two symmetric portions of the beam. The crack propagation is described by means of the cohesive crack model. For the application of the numerical scheme, the symmetry cross section of the beam is subdivided into finite elements by n nodes. Consequently, cohesive stresses are replaced by equivalent nodal forces by integrating the corresponding distributed tractions over the element side. Such nodal forces depend on the nodal opening displacements according to the cohesive law shown in Fig. 16a. The nodal forces, F , acting along the mid-span cross section are computed as follows:

$$\{F\} = [K_w]\{w\} + \{K_p\}P, \tag{2}$$

where $\{F\}$ is the vector of nodal forces, $[K_w]$ is the matrix of the coefficients of influence for the nodal displacements, $\{w\}$ is the vector of nodal displacements, and $\{K_p\}$ is the vector of the coefficients of influence for the applied load P . All the coefficients of influence are computed a priori with a linear-elastic finite-element analysis (for more details see Ref. [31]). When fracturing takes place, the following equations hold for the real crack region, the fictitious crack zone and the elastic ligament, respectively (see Fig. 16b, where the central portion of the TPB specimen is shown):

$$F_i = 0 \quad \text{for } i = 1, 2, \dots, (j - 1), \tag{3a}$$

$$F_i = \max\left(F_u - (F_u - F_o) \frac{w}{w_o}; F_o \left(1 - \frac{w - w_o}{w_c - w_o}\right)\right) \quad \text{with } 0 < w < w_c, \quad \text{for } i = j, \dots, (m - 1), \tag{3b}$$

$$w_i = 0 \quad \text{for } i = m, \dots, n, \tag{3c}$$

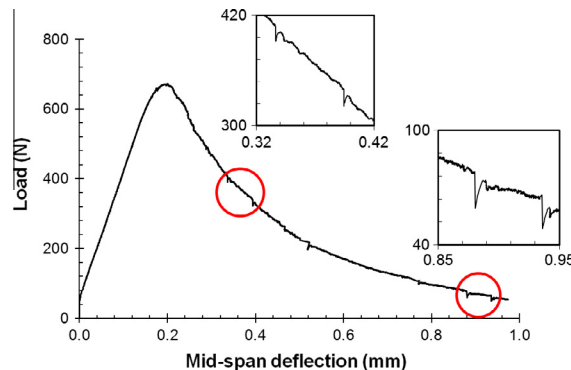


Fig. 14. Experimental load vs. mid-span deflection curve of Specimen B1, with magnification of some instabilities occurring in the post-peak regime.

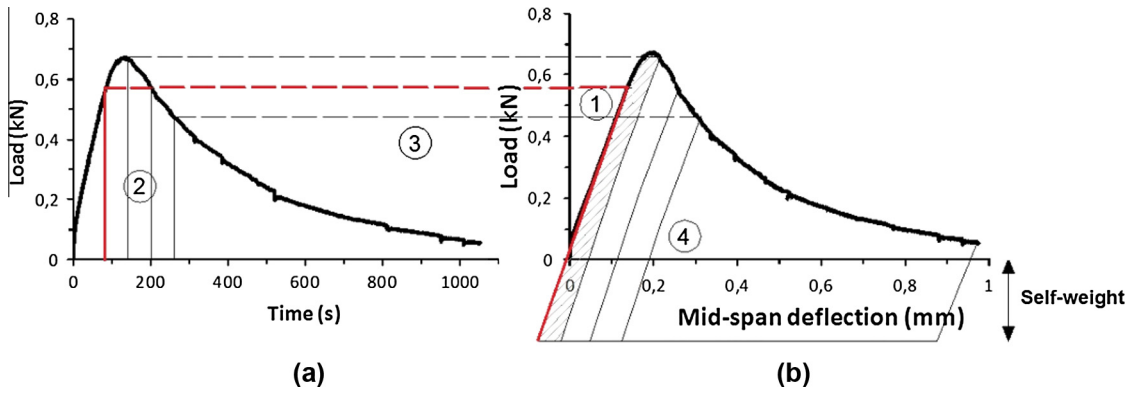


Fig. 15. Sketch of the procedure followed to compute the dissipated energy rate: (a) load–time and (b) load–displacement diagrams.

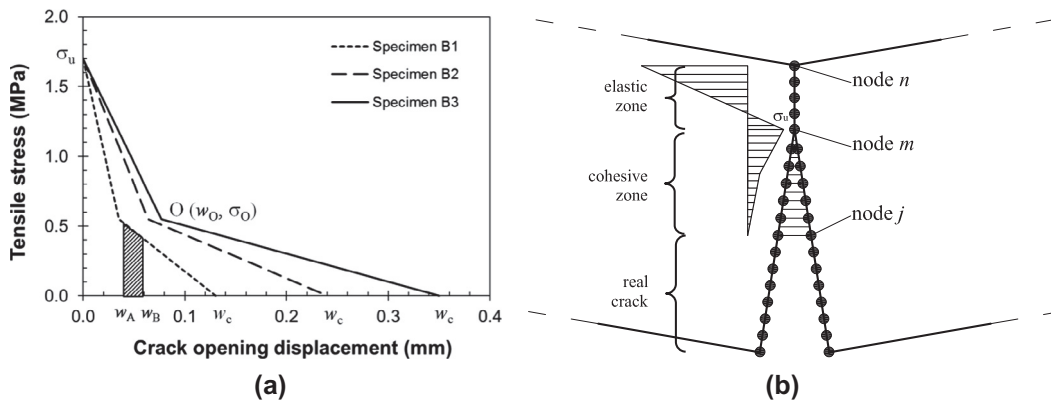


Fig. 16. (a) Cohesive constitutive laws for the three specimens; (b) model of the mid-span cross section with the corresponding stress distribution.

where F_u and F_0 are equal to the stresses σ_u and σ_0 multiplied by the distance between two consecutive nodes of the discretization. Eqs. (2) and (3) constitute an algebraic system of $(2n)$ equations with $(2n + 1)$ unknowns, i.e., the nodal displacements $\{w\}$, the nodal forces $\{F\}$, and the applied load P . In this case, since a strength criterion is adopted for crack propagation, an additional equation can be introduced to set the force in the fictitious crack tip, m , equal to the tensile ultimate force. Due to the nonlinear character of the problem, the Newton–Raphson iterative method is used to find the equilibrated solution at each loading step. The driving parameter of the process is the tip of the fictitious crack, that is moved from one node to the other of the discretization. At each step of the algorithm it is possible to calculate the deflection, δ , as follows:

$$\delta = \{D_w\}\{w\} + D_p P, \tag{4}$$

where $\{D_w\}$ is the vector of the coefficients of influence for the nodal displacements, and D_p is the coefficient of influence for the applied load.

As regards the numerical simulation, it is important to note that alternative computational methods, recently introduced and particularly suitable for the simulation of AE and damage dynamics as avalanche phenomena, do not use a set of differential or integral equations to describe the model in the space–time domain. Different methods have been implemented as a function of the considered individual elements, e.g., particles or bars. The process is called “Computational Mechanics of Discontinua” and it is now an integral part of cutting-edge research in different solid modeling fields [32]. Examples of this new type of approach are the models based on the discrete particles method, which were originally proposed in [33–36]; and the models made of bars linked at their nodes, which are known as lattice models. In the latter field, among others, the contributions by Hemmer and Hansen [37], Krajcinovic [38], Chakrabarti and Benguigui [39], and Rinaldi [40] have to be mentioned. Their models constitute a very interesting way to simulate the continuum, and provide qualitative information that shed light on the fracture behavior of quasi-brittle materials such as concrete and rocks. Taking into account discrete damage mechanics, lattice models are particularly suitable to reproduce the generation of AE events, arising from the materials, during the different stages of damage growth. These models are also fundamental for the application of advanced statistical methods and non-standard mathematical methods, e.g. fractal theory. In this field, some contributions have been published by the authors, in which the numerical simulations carried out with a truss-like Discrete Element Method and the experimental data appear to be in good agreement [41,42].

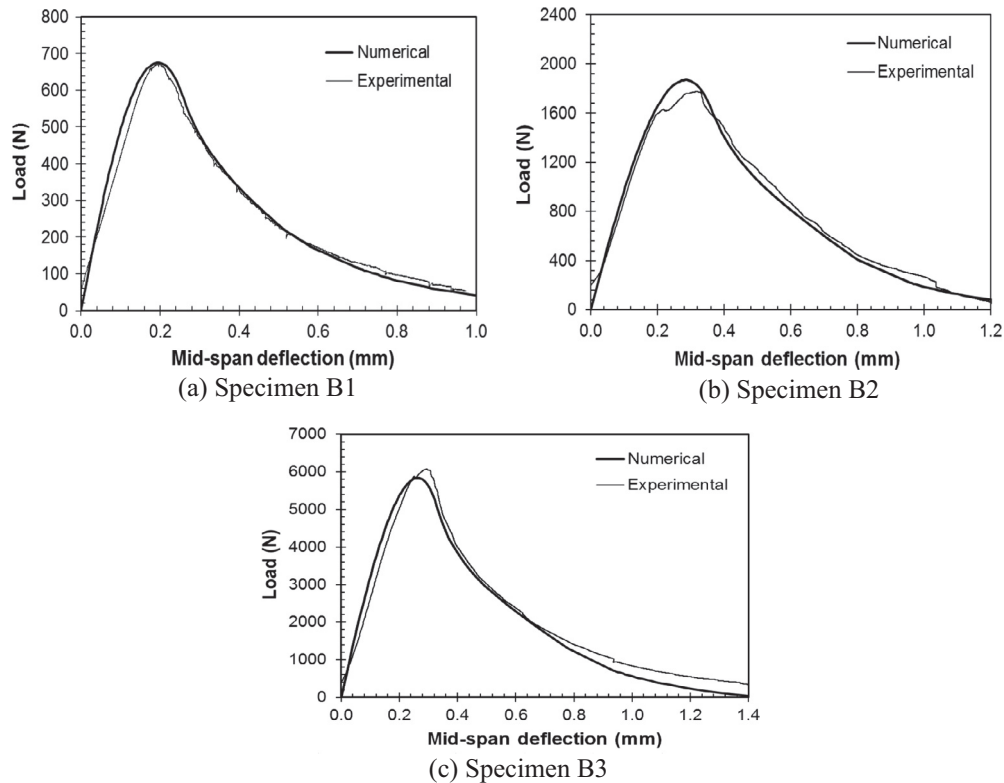
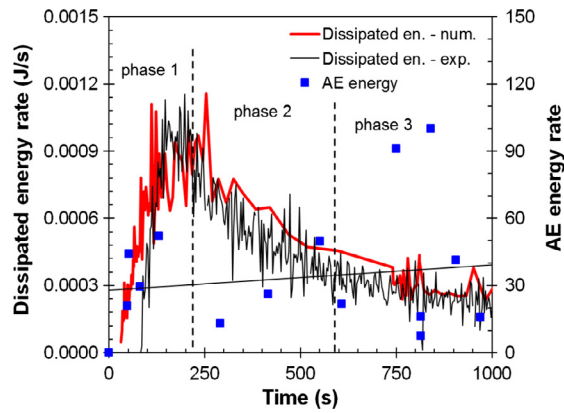


Fig. 17. Comparison between experimental load vs. displacement curves and corresponding numerical simulations for the three specimens.

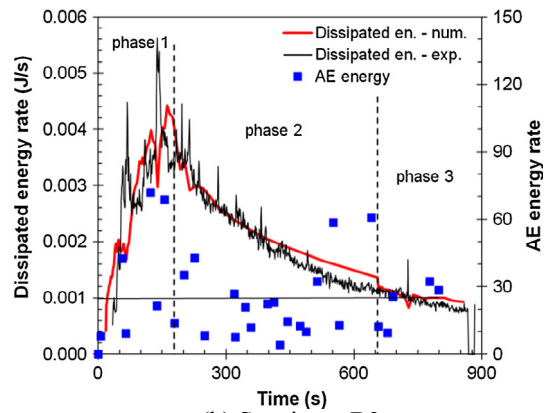
The algorithm herein applied permits to track step-by-step the crack propagation and to determine the corresponding resistant load and the mid-span deflection. Starting from the initial configuration (pre-notched concrete beam), the loading process is simulated by imposing a step-by-step crack tip propagation. At each step of calculation, the crack tip is advanced by a fixed amount and the load corresponding to the attainment of the critical condition for crack propagation, i.e. the tensile stress in the fictitious crack tip to be equal to the material strength, is sought. In a first stage, only the fictitious crack tip propagates, whereas the real crack tip starts to propagate only when the critical value defined by the cohesive crack law for the crack opening is overcome. The cohesive constitutive laws adopted for the simulations of the three specimens are shown in Fig. 16a. The tensile strength was assumed equal to 1.7 MPa for the three sizes, whereas the fracture energy was changed, according to the values obtained from the experimental tests. The shape of the cohesive laws was chosen as bilinear, whereas the values of the critical crack opening, w_c , and the position of the knee of the constitutive law, point O in Fig. 16a, were varied in order to optimize the fitting with the experimental load–displacement curves. The value of w_c is 0.13 mm, 0.24 mm and 0.35 mm for specimen B1, B2 and B3, respectively. The values of the crack opening displacement and the stress correspondent to point O are 0.035 mm and 0.55 MPa for Specimen B1, 0.064 mm and 0.55 MPa Specimen B2, and 0.077 mm and 0.55 MPa for Specimen B3. The load vs. deflection curves obtained from the simulations are compared to the experimental ones in Fig. 17.

The almost perfect agreement between numerical and experimental results in terms of the global response gives us the confidence that also the cracking behavior, i.e. the step-by-step crack propagation and the distributions of stresses and opening displacements along the crack, is close to reality. The evolution of the energy dissipation is therefore calculated on the basis of the numerical results. At each step of crack propagation, the dissipated energy can be precisely computed on the basis of the cohesive constitutive law. As an example, let us consider that at a given step of calculation the crack opening in correspondence of a point along the fictitious crack increases from w_A to w_B (see Fig. 16a). The corresponding energy per unit area dissipated by this point is therefore represented by the shaded area in the diagram in Fig. 16. The integration of such contributions over the total fictitious crack area gives the energy dissipated in the considered step. In order to evaluate the rate of the dissipated energy, the mid-span deflection axis has been converted into time, by comparison with the experimental results.

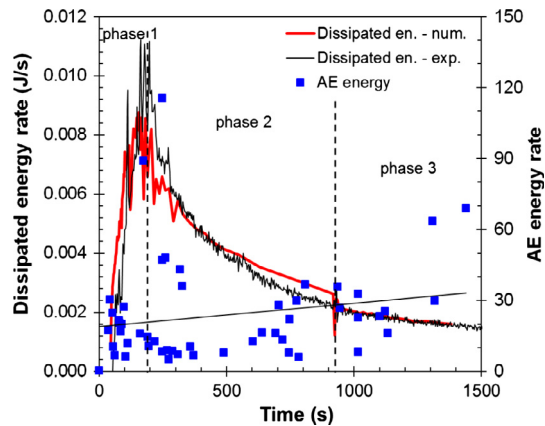
The computed energy rates for the three specimens are shown in Fig. 18, as a function of time. A good agreement has been obtained between experimentally and numerically evaluated dissipated energy rates, represented by thin black and thick red lines, respectively, further confirming the reliability of the numerical approach. These curves, even if highly irregular, evidence a clear trend for the dissipated energy rate, common to the three tests: it rapidly increases in the first part of the test,



(a) Specimen B1



(b) Specimen B2



(c) Specimen B3

Fig. 18. Energy dissipation rate and AE energy rate as a function of time for the three specimens.

when much energy is spent to create and increase the process zone (phase 1 in Fig. 18), then, it starts to decrease when the second part of the cohesive law (that with a lower slope) comes into play in the process zone (phase 2) and, finally, it continues to decrease when the real crack propagates with a consequent reduction of the process zone up to vanish at the complete failure of the specimen (phase 3). Even though the trend is similar for the three cases, the values of the rate increase by increasing the specimen size. As regards the emitted energy rate, a completely different behavior has been obtained. A strong oscillation of the values is evidenced during all the loading process, with a slight tendency to increase by approaching the

end of the test (see the thin straight line in Fig. 18, representing a linear interpolation of the data). Certainly, their trend is completely uncorrelated to that of the dissipated energy rate. Furthermore, the range of variation of the values is almost independent of the specimen size.

A similar behavior was observed also by Aggelis and co-workers [43] in steel fiber reinforced concrete (SFRC) and plain concrete beams, loaded under four-point bending test. In that work, following the ASTM C1609/C 1609M-05 rules, the beams toughness was calculated as the area under the load–deflection curve until the deflection of 2 mm. This energy was then compared with that obtained from AE monitoring. From this analysis it emerges that specimens with high toughness, i.e. high dissipated energy, are characterized by low cumulative AE energy, and vice versa. More precisely, the AE energy results to be inversely proportional to the area under the load–deflection curve. This behavior occurs both with SFRC and plain concrete. Moreover, plain concrete specimens exhibit larger stress-drops and higher amounts of emitted AE energy throughout their testing, compared to SFRC ones. As a matter of fact, in the presence of ductile fibers, a substantial part of energy is restrained in the form of plastic deformation. This leads to an increase of the dissipated energy and a decrease of the emitted energy recorded by the acoustic emission transducers.

5. Conclusions

The present paper discusses about the main AE parameters during fracture propagation in concrete members. From the analyses, the following conclusions may be drawn.

- (1) For all the beams tested in the TPB scheme a shift from higher to lower frequencies was observed by approaching the final stage of the loading process. Considering also that the RA values are commonly low, a dominance of tensile cracks (Mode I) was found.
- (2) As regards the specimen subjected to compression, the collapse was reached by different modalities of fracture. Mode I splitting failure dominates the initial mechanical response, whereas a crushing mode, characterized also by friction components (Mode II), appears by approaching the final stage. The clear differences between the two cases reinforce the effectiveness of the fracture mode identification by means of the AE analysis.
- (3) As regards the peak amplitude, a linear decrease proportional to the signal propagation length was found for the monitored beam specimens. The data are well fitted by a linear regression because the detected frequencies are relatively low, around 50–70 kHz, and the range of the propagation distances from the AE sources and the sensors is limited, from 40 to 400 mm. Obviously, the attenuation phenomena are reduced in laboratory specimens; whereas they have a greater effect on real structures where the propagation lengths of acoustic waves are longer. The sensors have to cover a larger area, therefore the AE parameters are subjected to a more evident attenuation mechanism. This phenomenon can be studied in the future to obtain correct results as regards the mode of cracking also for large structures.
- (4) For the three beams, the fracture energy and the energy of the AE signals were calculated according to the recommendations RILEM TC 50-FMC [23] and RILEM TC 212-ACD [9], respectively. A considerable increase in the fracture energy was evidenced by increasing the specimen size, whereas an opposite trend was obtained for the AE energy per surface unit (see Fig. 13 and Table 2). Such a discrepancy suggests that there is not a direct correlation between the two parameters. In fact, the AE energy is an emitted energy, consequent to a surplus of released energy with respect to the dissipated one. It is emitted in correspondence of snap-back instabilities. These instabilities mainly occur when the materials have a macrostructural catastrophic failure, such as the collapse of brittle rock specimens in compression [20]. However, local instabilities can develop also at a microscale level during a normal softening behavior, due to the fact that cracks grow discontinuously in correspondence to loading drops (see Fig. 2). The more pronounced the instabilities are, the higher the emitted energy is. Therefore, it can be concluded that the energy that is globally released during the loading process is partially dissipated to create the fracture surfaces, and partially transformed into emitted energy, which can be detected by the AE technique.
- (5) Finally, the differences between dissipated and emitted energy rates were analyzed on the basis of the evolution of these two quantities over the time, during the progress of the experimental test. A numerical simulation of the mechanical response of the TPB tests was performed by the cohesive crack model. Afterward, the computed experimental and numerical dissipated energy rates were compared to the AE energy rates detected by each sensor, as a function of time. From these analysis, it was possible to observe that the dissipation energy rate rapidly increases and reaches its maximum value around the peak load. During the softening phase the dissipation rate decreases up to the end of the test. As regards the AE energy rate, it slightly increases up to the end of the test. Therefore, this is a further confirmation that the two energies have a different origin and nature.

Acknowledgement

The authors gratefully acknowledge the support of ALCIATI Ltd (Vigliano d'Asti-Italy) for supplying the research materials.

References

- [1] Ohtsu M. The history and development of acoustic emission in concrete engineering. *Mag Concr Res* 1996;48:321–30.
- [2] Grosse C, Ohtsu M. *Acoustic emission testing*. Springer; 2008.
- [3] Carpinteri A, Lacidogna G, Pugno N. Structural damage diagnosis and life-time assessment by acoustic emission monitoring. *Engng Fract Mech* 2007;74:273–89.
- [4] Carpinteri A, Lacidogna G, Manuello A, Niccolini G. Acoustic emission wireless transmission system for structural and infrastructural networks. In: Van Mier JGM, Ruiz G, Andrade C, Yu RC, Zhang XX, editors. *Proc VIII international conference on fracture mechanics of concrete and concrete structures FraMCoS-8*, March 10–14, 2013, Toledo, Spain; 2013.
- [5] Scholz CH. The frequency-magnitude relation of microfracturing in rock and its relation to earthquakes. *Bull Seismol Soc Am* 1968;58:99–415.
- [6] Carpinteri A, Lacidogna G, Niccolini G, et al. Critical defect size distributions in concrete structures detected by the acoustic emission technique. *Meccanica* 2008;43:349–63.
- [7] Carpinteri A, Lacidogna G, Puzzi S. From criticality to final collapse: evolution of the b -value from 1.5 to 1.0. *Chaos, Solitons Fractals* 2009;41:843–53.
- [8] Aggelis DG, Mpalaskas AC, Ntalakas D, Matikas TE. Effect of wave distortion on acoustic emission characterization of cementitious materials. *Constr Build Mater* 2012;35:183–90.
- [9] Recommendation of RILEM TC 212-ACD. Acoustic emission and related NDE techniques for crack detection and damage evaluation in concrete: measurement method for acoustic emission signals in concrete. *Mater Struct* 2010;43:1177–81.
- [10] Recommendation of RILEM TC 212-ACD. Acoustic emission and related NDE techniques for crack detection and damage evaluation in concrete: test method for damage qualification of reinforced concrete beams by acoustic emission. *Mater Struct* 2010;43:1183–6.
- [11] Recommendation of RILEM TC 212-ACD. Acoustic emission and related NDE techniques for crack detection and damage evaluation in concrete: test method for classification of active cracks in concrete by acoustic emission. *Mater Struct* 2010;43:1187–9.
- [12] Soulioti D, Barkoula NM, Paipetis A, Matikas TE, Shiotani T, Aggelis DG. Acoustic emission behavior of steel fibre reinforced concrete under bending. *Constr Build Mater* 2009;23:3532–6.
- [13] Ohno K, Ohtsu M. Crack classification in concrete based on acoustic emission. *Constr Build Mater* 2010;24:2339–46.
- [14] Aggelis DG. Classification of cracking mode in concrete by acoustic emission parameters. *Mech Res Commun* 2011;38:153–7.
- [15] Aldahdooh MAA, Bunnori N, Muhammad. Crack classification in reinforced concrete beams with varying thicknesses by mean of acoustic emission signal features. *Constr Build Mater* 2013;45:282–8.
- [16] Landis EN, Shah SP. Frequency-dependent stress wave attenuation in cement-based materials. *J Engng Mech* 1995;121:737–43.
- [17] Carpinteri A, Corrado M, Lacidogna G. Three different approaches for damage domain characterization in disordered materials: fractal energy density, b -value statistics, renormalization group theory. *Mech Mater* 2012;53:15–28.
- [18] Muralidhara S, Prasad BK, Raghunath H, Karihaloo BL. Fracture process zone size and true fracture energy of concrete using acoustic emission. *Constr Build Mater* 2010;24:479–86.
- [19] Landis EN, Baillon L. Experiments to relate acoustic emission energy to fracture energy of concrete. *J Engng Mech (ASCE)* 2002;128:698–702.
- [20] Carpinteri A, Corrado M, Lacidogna G. Heterogeneous materials in compression: correlations between absorbed, released and acoustic emission energies. *Engng Failure Anal* 2013;33:236–50.
- [21] Carpinteri A, Monetto I. Snap-back analysis of fracture evolution in multi-cracked solids using boundary element method. *Int J Fract* 1999;98:225–41.
- [22] Carpinteri A, Massabò R. Continuous vs discontinuous bridged-crack model for fiber-reinforced materials in flexure. *Int J Solids Struct* 1997;34:2321–38.
- [23] Recommendation of RILEM TC 50-FMC. Determination of the fracture energy of mortar and concrete by means of three point bend tests on notched beams. Draft recommendation. *Mater Struct* 1985;18:286–90.
- [24] Zhou J. A study of acoustic emission technique for concrete damage detection. Master's report, Michigan Technological University; 2011. <http://digitalcommons.mtu.edu/etds/7>.
- [25] Ohno K, Uji K, Ueno A, Ohtsu M. Fracture process zone in notched concrete beam under three-point bending by acoustic emission. *Constr Build Mater* 2014;67:139–45.
- [26] Kao CS, Carvalho FCS, Labuz JF. Micromechanisms of fracture from acoustic emission. *Int J Rock Mech Min Sci* 2011;48:666–73.
- [27] Carpinteri A, Chiaia B. Size effects on concrete fracture energy: dimensional transition from order to disorder. *Mater Struct* 1996;29:259–66.
- [28] Carpinteri A, Ferro G. Scaling behavior and dual renormalization of experimental tensile softening responses. *Mater Struct* 1998;31:303–9.
- [29] Carpinteri A. Size effects on strength, toughness, and ductility. *J Engng Mech, ASCE* 1989;115:1375–92.
- [30] Carpinteri A, Corrado M, Mancini G, Paggi M. Size-scale effects on plastic rotational capacity of reinforced concrete beams. *ACI Struct J* 2009;106:887–96.
- [31] Carpinteri A, Corrado M, Paggi M. An integrated cohesive/overlapping crack model for the analysis of flexural cracking and crushing in RC beams. *Int J Fract* 2010;161:161–73.
- [32] Munjiza A (Ed). Special issue on the discrete element method: aspects of recent developments in computational mechanics of discontinua. *Engng Comput* 2009;26:578–743.
- [33] Brara A, Camborde F, Klepaczko JR, Mariotti C. Experimental and numerical study of concrete at high strain rates in tension. *Mech Mater* 2001;33:33–45.
- [34] Munjiza A, Bangash T, John NWM. The combined finite-discrete element method for structural failure and collapse. *Engng Fract Mech* 2004;71:469–83.
- [35] Rabczuk T, Belytschko T. A three-dimensional large deformation meshfree method for arbitrary evolving cracks. *Comput Methods Appl Mech Engng* 2007;196:2777–99.
- [36] Rabczuk T, Bordas S, Zi G. A three-dimensional meshfree method for continuous multiple-crack initiation, nucleation and propagation in statics and dynamics. *Comput Mech* 2007;40:473–95.
- [37] Hemmer C, Hansen A. The distribution of simultaneous fiber failure in fiber bundles. *J Appl Mech* 1992;59:909–14.
- [38] Krajcinovic D. *Damage mechanics*. Amsterdam: Elsevier; 1996.
- [39] Chakrabarti BK, Benguigui LG. *Statistical physics of fracture and breakdown in disordered systems*. Oxford: Clarendon Press; 1997.
- [40] Rinaldi A. Advances in statistical damage mechanics (SDM): new modelling strategies. In: Voyiadjis G, editor. *Damage mechanics and micromechanics of localized fracture phenomena in inelastic solids*. CISM Course Series, Springer; 2011. p. 105–224.
- [41] Iturrioz I, Lacidogna G, Carpinteri A. Experimental analysis and truss-like discrete element model simulation of concrete specimens under uniaxial compression. *Engng Fract Mech* 2013;110:81–98.
- [42] Iturrioz I, Lacidogna G, Carpinteri A. Acoustic emission detection in concrete specimens: experimental analysis and lattice model simulations. *Int J Damage Mech* 2014;2:327–58.
- [43] Aggelis DG, Soulioti DV, Gatselou EA, Barkoula NM, Matikas TE. Monitoring of the mechanical behavior of concrete with chemically treated steel fibers by acoustic emission. *Constr Build Mater* 2013;48:1255–60.